Available online at www.sciencedirect.com
SCIENCE DIRECT®
International Journal of Heat and Mass Transfer 49 (2006) 3514–3529
International Journal of HEAT and MASS TRANSFER
www.elsevier.com/locate/ijhmt

Structure of turbulent heat flux in a flow over a heated wavy wall

Nils Kruse, Philipp Rudolf von Rohr *

Institute of Process Engineering, ETH Zurich, 8092 Zurich, Switzerland

Received 16 June 2005; received in revised form 2 February 2006
Available online 19 May 2006

Abstract

A particle image thermometry technique is proposed to determine the turbulent heat flux in a water channel between a sinusoidal heated bottom and a flat top wall. Reynolds numbers between 2400 and 20,500 are considered. A proper orthogonal decomposition of combined velocity and temperature fields reveals a quantitative agreement between large-scale thermal and momentum structures. The distribution of budget terms of the streamwise and wall-normal heat fluxes are similar to those for the two Reynolds stress components. Co-spectra indicate that larger scale structures make a significant contribution to the streamwise heat flux and smaller scales are more important to the wall-normal heat flux.

Keywords: Particle image thermometry; Heat flux; Wavy wall; Turbulent flow

1. Introduction

Current engineering turbulent heat transfer computations rely on various one-point closure turbulence models. Among them those based on second-moment equations are of great interest for many researchers [1]. The second-moment equations contain several terms of unknown correlations and higher order moments, which must be modeled with unknown variables. The value of computational methods highly depends on how well the various scalar transport processes are characterized in the closure models. The mathematical model must account for both the turbulent stresses, $\overline{u_i'u_j'}$, and heat fluxes, $\overline{u_i'T'}$. To define the turbulent heat flux in the Reynolds averaged energy equation, to describe the inter-relation between heat and momentum transfer and to investigate the role of large-scale structures with respect to heat transport, the combined behavior of the instantaneous local flow and the corresponding instantaneous heat transfer must be understood.

Investigating the turbulent heat flux requires a measurement technique that is capable of recording simultaneously the velocity and temperature field, and resolving both spatial and temporal scales. It has been mostly studied by intrusive point-wise measurement techniques (e.g. [2]). Single point measurements are normally performed using a combination of a hot-wire and cold-wire probe. The resulting data recorded are often reported as time-averaged information, which makes it difficult to establish the presence and characteristics of transient flow structures. An alternative method is an optical technique called digital particle image thermometry. The technique has been employed by Dabiri and Gharib [3] to study the temperature distribution of a heated laminar vortex ring. The main advantage of this method is that velocity and temperature of a whole field can be measured instantaneously.

We address a novel measurement technique to propose spatially resolving and simultaneous measurements of the velocity and a scalar. Dominant scales in the velocity and temperature field are obtained from a proper orthogonal decomposition (POD) analysis. A constant heat flux is provided by the manganin covered wavy surface as a function of current, I. A Reynolds number scaling factor of 8.5 is considered. Fig. 1 shows the coordinate system and schematically illustrates characteristic regions of the mean flow field in the vicinity of the wavy surface. Coordinate x is

* Corresponding author. Tel.: +41 1632 2488; fax: +41 1633 1119.
E-mail address: vonrohr@ipe.mavt.ethz.ch (P. Rudolf von Rohr).

0017-9310/$ - see front matter © 2006 Elsevier Ltd. All rights reserved.
doi:10.1016/j.ijheatmasstransfer.2006.03.003

Nomenclature

a	half-amplitude of the wave profile (m)
a_i	coefficient in the proper orthogonal decomposition (–)
A	cross-sectional area (m^2)
A	matrix (–)
B	channel width (m)
$\mathbf{B}$	blue light intensity, $m_{pix} \times n_{pix}$ matrix (–)
c_p	specific heat capacity at constant pressure (kJ/(kg K))
$\mathbf{C}$	$M \times N$ covariance matrix (–)
d_p	particle diameter (m)
E	energy (–)
E_{tk}	turbulent kinetic energy production (m^2/s^3)
$\mathbf{G}$	green light intensity, $m_{pix} \times n_{pix}$ matrix (–)
h	half channel height (m)
H	full channel height (m)
$\mathbf{H}$	hue, matrix $m_{pix} \times n_{pix}$ (raw data) or $m \times n$ (locally averaged) (–)
i, j, k, l	integer counters (–)
I	current (A)
$\mathbf{I}$	intensity, $1/3(\mathbf{R}+\mathbf{G}+\mathbf{B})$, $m_{pix} \times n_{pix}$ matrix (raw data) (–)
k	turbulent kinetic energy (m^2/s^2)
m	liquid mass (kg)
m	number of (locally averaged) temperature and velocity locations in the horizontal direction of a rectangular 2-D domain (–)
m_{pix}	number of pixels on CCD chip (horizontal) (–)
M	magnification factor, number of temperature or velocity fields (–)
n	number of (locally averaged) temperature and velocity locations in the vertical direction of a rectangular 2-D domain (–)
n	POD mode (–)
n_{pix}	number of pixels on CCD chip (vertical) (–)
N	spatial dimension of dataset for POD analysis, for 2-D analysis: $n \cdot m$ (–)
P	turbulent production term (–)
Pr	Prandtl number, ν/κ (–)
$\mathbf{R}$	red light intensity, $m_{pix} \times n_{pix}$ matrix, $N \times N$ cross-correlation matrix (–)
$\dot{q}_w$	specific wall heat flux (W/m^2)
R	resistance (Ω)
R_{ij}	correlation function (–)
Re	Reynolds number (–)
Re_h	Reynolds number for channel flow, $U_b h/\nu$ (–)
$\mathbf{S}$	saturation, $m_{pix} \times n_{pix}$ matrix (raw data) (–)
t	time coordinate (s)
T	turbulent transport term (–)
T	fluid temperature (K)
T_w	wall temperature (K)
T_∞	bulk temperature (K)
T_b	bulk temperature (channel flow) (K)
u, v, w	components of the instantaneous fluid velocity (m/s)
U	voltage (V)
U	mean streamwise velocity (m/s)
U_b	bulk velocity (channel flow) (m/s)
$\mathbf{U}$	set of u-velocities in the (x,z)-plane, $N \times M$ matrix (–)
$\mathbf{V}$	set of u-velocities in the (x,z)-plane, $N \times M$ matrix (–)
x, y, z	Eulerian Cartesian coordinates (m)
$\mathbf{X}$	set of spatio-temporal data, $N \times M$ matrix (–)
y_w	profile of the wavy bottom wall (m)

Greek symbols

α	amplitude-to-wavelength ratio, $2a/\Lambda$ (–)
α	heat transfer coefficient ($W/(m^2\,K)$)
β	thermal expansion coefficient (K^{-1})
δ_{LS}	light sheet thickness (k)
ϑ	Celsius temperature (C)
κ	thermal diffusivity (m^2/s)
λ	light wavelength (m)
λ	thermal conductivity (W/(m K))
λ_n	eigenvalue of POD mode n (–)
Λ	wavelength of the sinusoidal profile at the bottom wall (m)
Λ_z	characteristic scale in the spanwise direction (m)
μ	dynamic viscosity (kg/(m s))
ν	kinematic viscosity (m^2/s)
$\mathbf{\Pi}_i$	eigenfunction, $N \times 1$ matrix (–)
ϱ	fluid density (kg/m^3)
ϱ_p	particle density (kg/m^3)

Abbreviations

CCD	charge coupled device
CL2	Craik–Leibovich type 2 instabilities
CT	color temperature
DC	direct current
FOV	field of view
LC	liquid crystals
LDV	laser Doppler velocimetry
Nd:YAG	neodymium:yttrium aluminium garnet ($Y_3Al_5O_{12}$) crystal
$\mathcal{O}\{\cdot\}$	order of $\{\cdot\}$
PIT	particle image thermometry
PIV	particle image velocimetry
pix	pixel
POD	proper orthogonal decomposition
PVC	poly vinyl chloride
RMS	root mean square
TLC	thermochromic liquid crystals
WB	white balance
2-D	two-dimensional
3-D	three-dimensional

$\overline{(\cdot)}$	time average	i	running index
$(\cdot)'$	fluctuation of $(\cdot), (\cdot) - \overline{(\cdot)}$	j	running index
$\langle\cdot\rangle$	spatial average	max	maximum value
$\langle\cdot,\cdot\rangle$	Euclidean inner product	mean	mean value
		rms	root-mean-square
Subscripts and superscripts		Λ	wavelength used as length scale
b	bulk quantity	∞	free stream
eff	effective temperature range	*	dimensionless value
h	half channel height (used as length scale)		

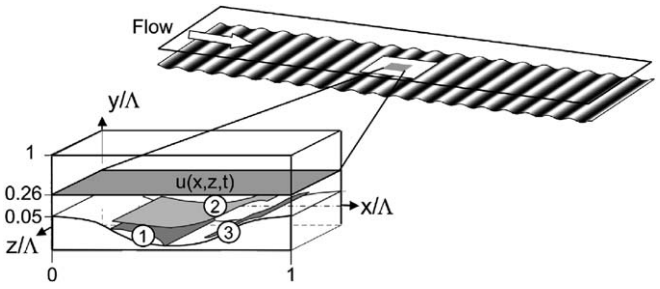

Fig. 1. Coordinate system and schematic of (1) the separation region, and the regions (2) of maximum positive and (3) negative Reynolds shear stress.

directed parallel to the mean flow, y is perpendicular to the top wall and z is the spanwise coordinate. The corresponding velocity components are denoted as u, v, and w. A separation zone (1), bounded by the isosurface of the mean streamfunction $\Psi(x,y) = 0$, is located in the wave troughs. At the uphill side, two regions of maximum (2) and minimum (3) Reynolds shear stress, $-\varrho\overline{u'v'}$, are found. The developed turbulent flow is characterized by the ratio of the amplitude, $2a$, to the wavelength of the wavy bottom wall, $\alpha = 2a/\Lambda = 0.1$ ($\Lambda = 30$ mm), and the Reynolds number:

$$Re_h = \frac{U_b \cdot h}{\nu}, \tag{1}$$

where ν denotes the kinematic viscosity, and h is the half-height of the channel. The bulk velocity U_b is defined as

$$U_b = \frac{1}{2h - y_w}\int_{y_w}^{2h} U(x_\xi, y)\,dy, \tag{2}$$

where x_ξ denotes an arbitrary x-location and $y_w(x) = 0.05\Lambda\cos(x \cdot 2\pi/\Lambda)$ describes the profile of the wavy surface. Reynolds averaging is used to decompose the velocity and the temperature into a mean and a fluctuating part, $u = \overline{u} + u'$ and $T = \overline{T} + T'$.

2. Experimental aspects

Measurements are carried out in a channel facility with deionized and filtered water as working fluid. The flow loop and frequency controlled pumps are designed for turbulence measurements at Reynolds numbers up to 21,000 with light sheet techniques. The volume of working fluid is approximately 0.280 m^3. The entire facility is made of black anodized aluminum, PVC, and Schott BK-7 glass. For a detailed description we refer to [3–5].

2.1. Channel facility and test section

The full height of the channel, H, is 30 mm, and its aspect ratio, B/H, is 12:1. The wavelength Λ of the sinusoidal wall profile is equal to the channel height. Optical access is provided at four streamwise locations of the wavy channel section through viewports at both side walls and at the flat top wall. Measurements are performed for a hydrodynamically developed flow after the 50th wave crest. The maximum field of view (FOV) of the top windows is 3.3Λ (streamwise) $\times$ 3.3Λ (spanwise). To determine the fluid viscosity, the water temperature is monitored downstream of the test section.

2.2. Resistively heated wall section

In order to provide constant heat flux boundary condition, the wavy PVC bottom wall is covered with a thin layer of manganin foil and can be heated resistively. A manganin foil of 1000 mm length, L_M, and 300 mm width, B_M, with a uniform thickness of 45 μm is used. Manganin is a copper–manganese–nickel (CuMnNi) alloy and characterized by a moderate specific electric resistance, $\varrho_{el,M}$, of 0.43 Ω mm^2 m^{-1} at 20 °C that is almost independent of the temperature. The resistivity is given by

$$R_M = \frac{\varrho_{el,M} L_M}{A_M}, \tag{3}$$

where L_M denotes the free length of the manganin layer between the two electrodes and is measured along the wavy profile. The cross-section of the foil, A_M, is equal 0.045×300 mm^2. Its resistance is therefore 36.6 m Ω. At both ends, the foil is soldered to copper electrodes. The electrodes are flush-mounted to the PVC bottom wall and connected to a welding transformer with a maximum direct current (DC) of 380 A. The manganin foil is attached to a milled PVC wavy wall segment with a two component adhesive (Degussa product Agomet F310). The electric circuit is shown in Fig. 2. The majority of the current, I, heats

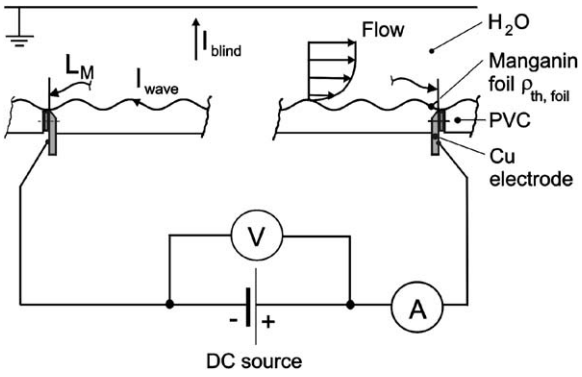

Fig. 2. Electric circuit to heat the manganin foil.

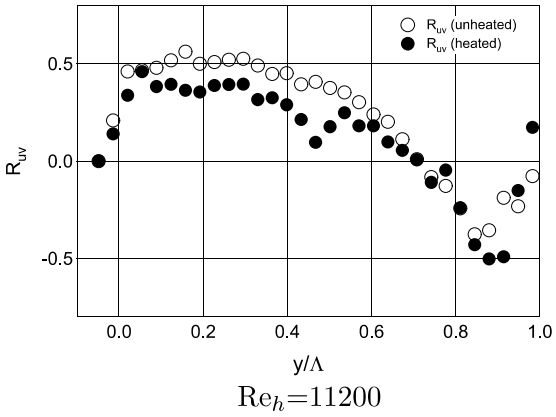

Fig. 3. Comparison of cross-correlation coefficients of the velocity fluctuation intensities, R_{uv}, under isothermal and non-isothermal conditions, $x/\Lambda = 0.5$, $Pr = 4.83$, $I = 220$ A.

the wave section, I_{wave}, where a fraction of it travels as a blind current through the working fluid. To decrease this effect, deionized water is used (Millipore RO 10 Plus). The water conductivity is monitored during the experiments. For a neglected blind current, the resulting heat flux is obtained by the resistance of the foil and the measured current:

$$Q = R_{\text{M}} I^2. \tag{4}$$

Blind currents flow between the manganin foil and the grounded aluminum top wall and can be estimated if the specific resistance of the water is known. For the used deionized water, $\varrho_{\text{el,H}_2\text{O}} = 200\ \Omega\,\text{m}$ is a typical value measured with a resistivity probe; for tap water it is approximately $20\ \Omega\,\text{m}$. Since the PVC bottom wall is characterized by a very high specific electric resistance of $\varrho_{\text{PVC}} = 10^{13}\ \Omega\,\text{m}$, the electric losses through it can be neglected. With the voltage U applied at both ends of the foil, the foil width, B_{M}, the channel height, H, and the length of the foil, L_{M}, we obtain for the ratio between the power loss due to the blind current, Q_{blind}, and the heating power at the wall surface, Q_{w}:

$$\frac{Q_{\text{blind}}}{Q_{\text{w}}} = \frac{U^2 B_{\text{M}} L_{\text{M}}}{3\varrho_{\text{el,H}_2\text{O}} H}. \tag{5}$$

At a direct current of 200 A, one obtains a relative loss of heating power of 0.014% for the de-ionized water, an 0.14% for tap water, which is smaller than the uncertainty of the temperature and velocity measurements. For the known resistance R_{M}, we therefore conclude to the heating power Q_{w} by measuring the direct current. For most numerical experiments, where turbulent flow studies are extended towards scalar transport, a passive scalar is considered, i.e. the temperature dependency of the fluid properties is neglected. However, for real fluid systems, a temperature dependency of the fluid properties exists. The measurements are performed with the lowest possible heat flux to meet the condition for the smallest effective temperature range of the thermochromic liquid crystals (TLC). Hence, we expect the fluid motion due to buoyancy to be negligible. To verify this assumption, the cross-correlation coefficients of the streamwise and wall-normal velocity fluctuation intensities, R_{uv}, are calculated and compared for the heated and unheated flow case. The cross-correlation coefficient indicates the degree of similarity in waveforms and differences in phase between two quantities and it is defined as

$$R_{u_i u_j} = \frac{\overline{u_i' u_j'}}{\sqrt{\overline{u_i'^2}}\sqrt{\overline{u_j'^2}}}. \tag{6}$$

Fig. 3 shows the coefficients in wall-normal direction at $Re_{\text{h}} = 11{,}200$. The good agreement between the cross-correlation coefficients for the unheated and heated flow indicates that the flow patterns are not seriously affected by the small effect of buoyancy. Using a moderate heating power and a small effective temperature sensitive range of the LCT formulation ($\Delta T_{\text{eff}} = 0.5\ \text{K}/1\ \text{K}$), the effect of fluid motion due to buoyancy, i.e. natural convection, is almost negligible and can be closely approximated by the transport of a passive scalar, most notably in the outer flow and at Reynolds numbers larger than 2400.

2.3. Experimental setup for simultaneous temperature and velocity measurements

The experimental arrangement is shown in Fig. 4. We use digital particle image velocimetry (PIV) [7–9] and liquid crystal thermometry (LCT) [6,10,11] simultaneously to determine the velocity and temperature field in a 2-D plane of the flow. LCT was found advantageous for measurements at flow fields that are characterized by small spatial variations of the fluid temperature in the image plane, i.e. for forced convective flows. The PIV measurement system consists of a laser, laser optics and a 12 bit monochrome camera with a resolution of 1280×1024 pixels^2. A flash-lamp-pumped dual Nd:YAG laser provides the pulse light source. Within the same FOV, a 3-CCD digital camera with NTSC color filters and a white balance (WB) of 5600K (Sony DXC-9100P) acquires the spatial color distribution of fluid-dispersed liquid crystal particles illuminated by a pulsed sheet of white light. The 3-CCD camera has a

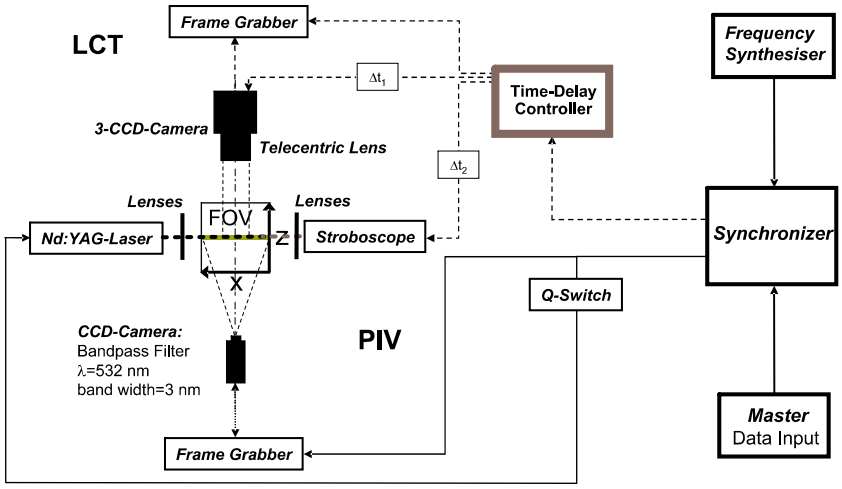

Fig. 4. Combined digital particle image velocimetry (PIV) and liquid crystal thermometry (LCT) approach to access the turbulent heat flux, $-\varrho\overline{u_i'T'}$, in a developed turbulent flow over heated waves.

pixel resolution of 768×572 pixel^2 for each chip and a FOV of $1.2\Lambda \times 0.83\Lambda$. The polychromatic white light source emits its intensity over a frequency band. A telecentric lens eliminates the sensitivity of the LCT technique on the viewing angle [12]. We use a white-light sheet from a stroboscope with a maximum power output of 3 Joule per pulse (Drelloscop 250, Drello) and a spectral range of $\lambda_S = 300 \ldots 1100$ nm. The light sheet thickness, produced by a fiberoptic line converter, is adjusted to approximately 2 mm with a lens aperture. A bandpass-filter is used on the monochrome camera ($\lambda = 532$ nm, bandwidth $\lambda_b = 3$ nm) in order to avoid overexposure from scattering light of the white light source. Measurements are taken in the (x, z)-plane at the vertical coordinate $y/H = 0.26$. Both systems are mounted on a traversing system to adjust the y-position with an accuracy of approximately 10 μm. We choose TLC particles with a temperature sensitive range of $\Delta T = 0.5$ K ($\Delta T = 1.0$ K) and particle diameter of $d_p = 14$ μm ($d_p = 16$ μm). A particle diameter smaller than the size of one CCD pixel does not imply disadvantages for measuring fluid temperatures, but restricts the accuracy of obtaining simultaneously the velocity fields through local cross-correlation of subsequent digital images [7]. For measurements in this study, the digital particle images are presented by more than one pixel in order to avoid undersampling.

2.4. Color calibration of liquid crystals

An accurate temperature calibration of the fluid-dispersed, encapsulated TLC (Formulation BM/R30C1W, Hallcrest) is an important prerequisite for quantitative LCT measurements. The liquid crystals used are of chiral nematic type and encapsulated to particles of diameter 20 μm. As the specific gravity of the encapsulated liquid crystal particles of 1020 kg/m^3 is close to water, the sedimentation effect is limited. The effective temperature sensitive range of the TLC formulation is $\Delta T = 1$ K. The color-to-temperature conversion for quantifying the visualized images is carried out with the calibrated relationship between the color and temperature using a spline fitting technique described by Funatani et al. [13]. The calibration of the TLC formulation is performed in a thermally stratified layer and described by Kruse [6] and Günther and Rudolf von Rohr [12].

2.5. Triggering

The triggering of the particle illumination by stroboscope and Nd:YAG laser and the imaging by the CCD monochrome and 3-CCD color camera are controlled by a software operated microcontroller (Model PIC16C73, Microchip). The system is triggered using 5 V TTL pulses. The measurement routine starts by a trigger signal from a frequency synthesizer to the synchronizer of the PIV system. When the trigger signal comes in, the PIV system (camera and laser) starts to operate in the preset mode. The same signal goes at the same time to the microcontroller, which generates a trigger input signal for the 3-CCD camera, the camera framegrabber and the stroboscope (LCT cycle), precisely adjusted to the PIV-time-cycle of Nd:YAG laser and monochrome camera. In order to prevent overexposure from the Nd:YAG laser pulse to the 3-CCD chip, the LCT cycle is delayed within the Kolmogorov time scale. The time delay controller guarantees the precise adjustment of delay times between all components within each cycle.

2.6. Time-delay microcontroller

The microcontroller operates as a synchronizing interface between the PIV-system (synchronizer, monochrome camera, Nd:YAG laser) and the LCT-system (3-CCD camera, stroboscope) in a master–slave computer arrangement.

A software tool (timing dialog box) linked from the Communication Port (Com Port) of a personal computer (“slave”) to the Com Port of the microcontroller contains the operating parameters. The timing dialog includes time delays between the reference TTL-signal to the synchronizer of the PIV-system (“master” system) and the LCT-system components. The trigger pulse is adjustable to a length of time of $1 \ldots 50$ ms, and a variable voltage of $U_T = 5/9$ V (resistance $R_T = 100\ \Omega$). The synchronizer coordinates the operation and timing of the PIV-system. The communication between the master computer and the synchronizer is controlled by using RS-232 commands. The interface allows a minimal time delay Δt_i of 0.1 ms. The 3-CCD camera, stroboscope and synchronizer receive a TTL-output signal from the microcontroller. The microcontroller is operated by a frequency synthesizer. That ensures a source trigger signal of highest accuracy during the whole measurement time. The TTL-signals are set to a standard polarity. The timing is set to the rising edge.

The timing master of the PIV-system is set to start with an incoming external trigger signal. The commercial software package Optimas 6.5 (Media Cybernetics, Inc.) running on the “slave”-computer is used for 3-CCD camera image acquisition. The 3-CCD camera records an image when the TTL trigger signal from the mircocontroller comes in. Whenever an external pulse is input, the image is captured to the memory replacing the previously captured image. Synchronizing signals from an Optimas macro control the time-delay procedure between exposure and image shifting from the camera to the 4 MB dualported memory framegrabber board (ITI model IC4-RGB), where the image is digitized and downloaded to the RAM of the personal computer. That ensures time-consistent operating conditions at high frequency rates. The Optimas macro itself is triggered by an ASCII-signal from the microcontroller.

Since the time delay between the 3-CCD camera exposure stroboscope flash is undetermined, a second time delay is used in order to synchronize the 3-CCD camera exposure and the stroboscope flash (flashlamp exposure duration $\Delta t_{\text{flash}} = 5\ \mu$s).

2.7. Experimental procedures

Measurements are taken at a location after the 50th wave crest, where we expect a hydrodynamically developed flow. Through the resistance heater, the temperature of the working fluid in the channel, deionized water, is adjusted to a temperature that corresponds to the lower end of the temperature sensitive range, $T_{W,1} = 28.9$ °C, of the TLC formulation. Through a 0.5 mm feeding port that is located 1.5 m upstream of the measuring position in the channel top wall, a suspension of TLC particles and deionized water is fed to the working fluid and homogeneously distributed. After the water temperature in the non-heated channel has adjusted to the temperature $T_{W,1}$, the resistance heater is turned on. We consider ensembles of $M = 900$ realizations containing nine sequences of 100 consecutive fields acquired at 1 Hz. The resistance heater is turned off after completing one measurement series. By monitoring the exact water temperature, the minor temperature increase $\mathcal{O}\{0.02 - 0.06\ \text{K}\}$ of the working fluid caused by the constant heat flux is being compensated by a subsequent postprocessing procedure. After the water temperature in the channel has decreased to the starting temperature, the procedure is repeated for additional image sequences. The camera images are downloaded into the computer RAM and subsequently stored as RGB .tif-files (3×8 bit) and monochrome .tif-files (12 bit) on a local harddisk. For a known temperature calibration, such information can be used for obtaining simultaneously temperature and velocity in transient flows (Fig. 5).

2.8. Image processing

We obtain a band of dominant wavelengths reflected from the spherical TLC particles as a function of the local fluid temperature. The three CCD chips of the camera (768×572 pixels^2) transiently record separate color bands of the reflected light as analog RGB information. The size of one square pixel is $8.3 \times 8.3\ \mu\text{m}^2$. With a 4 MB dualported memory framegrabber board (ITI model IC4-RGB), the images are digitized and downloaded to the RAM of a personal computer, where the commercial software package Optimas 6.5 (Media Cybernetics, Inc.) is used for image acquisition.

The temperature fields are related to the RGB images. A linear transformation from red, R_{ij}, green, G_{ij}, and blue intensities, B_{ij} in the image plane $i: 1, \ldots, 768$ and $j: 1, \ldots, 572$ [3,14] is given by

$$\begin{bmatrix} v_{1,ij} \\ v_{2,ij} \\ I_{ij} \end{bmatrix} = \begin{bmatrix} 2/\sqrt{6} & -1/\sqrt{6} & -1/\sqrt{6} \\ 0 & 1/\sqrt{6} & -1/\sqrt{6} \\ 1/3 & 1/3 & 1/3 \end{bmatrix} \cdot \begin{bmatrix} R_{ij} \\ G_{ij} \\ B_{ij} \end{bmatrix}. \tag{7}$$

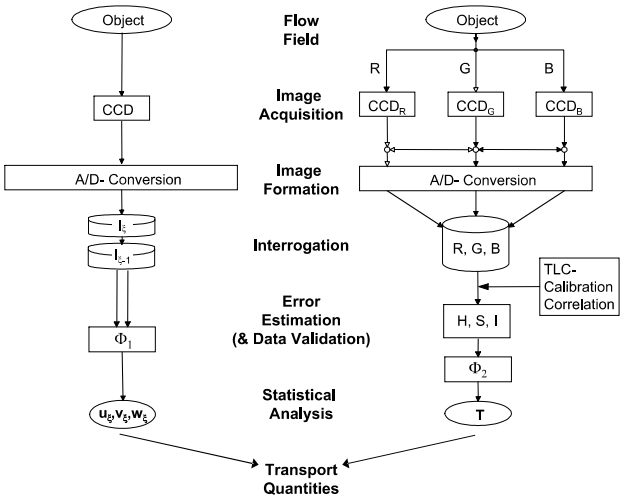

Fig. 5. Postprocessing procedure, stages of image formation, interrogation, and statistical analysis to obtain 2-D velocity ϕ_1 and temperature fields ϕ_2.

Table 1
Coefficients C_η of the 11th order polynomial

C_0	29.5183	C_4	−0.6053	C_8	−0.4839
C_1	0.4097	C_5	0.9602	C_9	0.0070
C_2	0.1890	C_6	0.8468	C_{10}	0.0984
C_3	−0.8204	C_7	−0.4033	C_{11}	0.0222

The local hue, H_{ij}, and the saturation, S_{ij}, are obtained by

$$H_{ij} = \begin{cases} \pi/2 - \tan^{-1}(v_{1,ij}/v_{2,ij}) : B_{ij} < G_{ij}, \\ \pi/2 + \tan^{-1}(v_{1,ij}/v_{2,ij}) : B_{ij} \geqslant G_{ij}, \end{cases} \tag{8}$$

$$S(i,j) = \sqrt{v_{1,ij}^2 + v_{2,ij}^2}. \tag{9}$$

The intensity variable, I, is the measure of the brightness of the light. The saturation, S, is the measure of the purity of the color. The hue value, H, is the measure of the color or the dominant wavelength of the light. In the HSI color system, H_{ij} defines an angle in the interval $[0, 2\pi]$. Three criteria are considered:

- $I_{ij} > \langle I \rangle_{ij}$, $\langle I \rangle_{ij}$ denotes an average over all pixels.
- $R_{ij} \vee G_{ij} \vee B_{ij} < 255$.
- $S_{ij} > S_{\min}$.

The first criterion implies that low-intensity background light is excluded, the second criterion disregards saturated pixels. The third criterion is applied to further minimize the contribution of white light. We consider only pixels which fulfill all criteria. From the validated hues, H_{ij}, local averages, H_{kl}, are calculated. A spot size of 40×30 pixels^2 is used.

The temperature measurements at the bottom wall and at the top wall are obtained from resistance thermometer readings. Small hues correspond to low fluid temperatures. The fluid temperature can be calculated from locally obtained hues using the polynomial:

$$\frac{T_{\text{poly}}}{^\circ\text{C}} = \sum_{\eta=0}^{11} C_\eta \cdot \langle H_{kl} \rangle_k^\eta, \tag{10}$$

with the coefficients summarized in Table 1.

The uncertainty of the hue angle, δH_l, can be calculated from the data [15] by

$$\delta H_l = 2\left[\frac{1}{m-1}\sum_{k=1}^{m}(H_{kl} - \langle H_{kl} \rangle_k)\right]^{0.5}, \tag{11}$$

where $\langle H_{kl} \rangle_k$ denotes a line-average (x-direction). If the polynomial in Eq. (10) is used, the uncertainty of the temperature prediction follows as

$$\delta T = \frac{\mathrm{d}T_{\text{poly}}}{\mathrm{d}H}\,\delta H_l. \tag{12}$$

3. Results in the (x, z)-plane

3.1. Instantaneous velocity and temperature fields

We consider an ensemble of $M = 900$ realizations containing nine sequences of 100 consecutive temperature and velocity fields acquired at Reynolds numbers of 2400, 5600, 11,200, 15,500 and 20,500.

Fig. 6 shows the dimensionless mean temperature and velocity distribution at a Reynolds number of 11,200. We consider a path in the channel center at a constant wall-normal distance of $y/\Lambda = 0.26$ in streamwise direction. Higher-temperature regions are mostly connected to lower-velocity structures and lower-temperature regions to higher-velocity structures. The high-temperature low-momentum structures develop when the fluid is partly decelerated by the wall shear and, at the same time, heated by the wall heat flux during the streamwise convection. The thermal structures are observed periodically in spanwise and elongated in streamwise direction, much the same as the momentum structures.

Simultaneous observations of wall thermal structures and flow patterns reveal large, longitudinal fluid columns in both fields. The magnitude of velocity and temperature fluctuation intensities increases with increasing Reynolds numbers by enhanced turbulent mixing. Structural information on the temperature and velocity fields and quantitative contributions of dominant scales are found by performing a statistical analysis.

3.2. Structural information from POD analysis

The proper orthogonal decomposition method (POD), proposed by Lumley [16], is generally accepted as the correct tool to decompose the quantitative flow field of a turbulent flow with spatially varying scales into characteristic modes [17]. The mathematical basis of POD is a Karhunen–Loève (KL) expansion. In the limit of two homogeneous flow directions, it is identical to a Fourier decomposition. Using this technique, the velocity field of a turbulent flow is decomposed into a series of eigenmodes

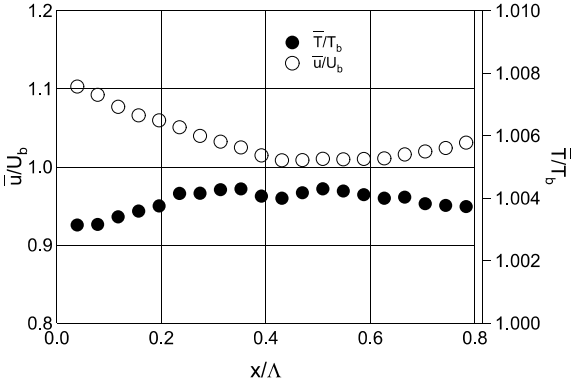

Fig. 6. Mean temperature and velocity distribution in streamwise direction, $z/B = 0.5$, $y/\Lambda = 0.26$, $Re_h = 11{,}200$, $Pr = 4.83$, $I = 220$ A.

(composed of eigenvalues and corresponding eigenfunctions) which represent the degree of kinetic energy associated with each supposed flow structure or flow mode comprising the flow. We use the method of snapshots [17,18] and perform a Karhunen–Loève (KL) or proper orthogonal decomposition (POD) on the streamwise velocity and temperature fields in the (x,z)-plane, $u'/U_b(x,y/\Lambda = 0.26,z,t)$ and $v'/U_b(x,y/\Lambda = 0.26,z,t)$, and temperature, $T'/T_b(x,y/\Lambda = 0.26,z,t)$.

We consider discrete times t_i with $i = 1,\ldots,M$, and $1,\ldots,N$ discrete locations within the (x,z)-plane, where $N = m \cdot n$ with $x : (1,m)$ and $z : (1,n)$. The resulting set of spatio-temporal data can be written as the $N \times M$ matrix:

$$\mathbf{U} = \{\mathbf{U}_i\}_{i=1}^{M} = \begin{bmatrix} u_{11}, u_{12}, \ldots, u_{1M} \\ u_{21}, u_{22}, \ldots, u_{2M} \\ \vdots \\ u_{N1}, u_{N2}, \ldots, u_{NM} \end{bmatrix} \tag{13}$$

with $\mathbf{U}_i = [u_1, u_2, \ldots, u_N]^T$. We obtain the mean streamwise velocity by averaging over the rows:

$$\overline{\mathbf{U}} = \frac{1}{M}\sum_{i=1}^{M}\mathbf{U}_i. \tag{14}$$

For the velocity fluctuations then follows:

$$\mathbf{U}_i' = \mathbf{U}_i - \overline{\mathbf{U}}, \quad i = 1,\ldots,M. \tag{15}$$

Using the method of snapshots, the $M \times M$ covariance matrix becomes:

$$\mathbf{C}_{ij} = \langle \mathbf{U}_i' \mathbf{U}_j' \rangle, \quad i,j = 1,\ldots,M, \tag{16}$$

where $\langle \cdot,\cdot \rangle$ is the Euclidean inner product. Since the matrix is symmetric its eigenvalues, λ_i, are nonnegative, and its eigenvectors, ϕ_i, $i = 1,\ldots,M$, form a complete orthogonal set. The orthogonal eigenfunctions are

$$\mathbf{\Pi}^{[k]} = \sum_{i=1}^{M}\phi_i^{[k]}\mathbf{U}_i', \quad k = 1,\ldots,M, \tag{17}$$

where $\phi_i^{[k]}$ is the ith component of the kth eigenvector.

We can associate energy with the velocity fluctuations and obtain, due to the orthogonality of the eigenfunctions [18,19]:

$$E = \sum_{i=1}^{M}\lambda_i. \tag{18}$$

The fractional contribution of one eigenfunction associated eigenvalue is

$$\frac{E_k}{E} = \frac{\lambda_k}{E}. \tag{19}$$

Fig. 7 presents the first three dominant streamwise velocity (first row) and fluid temperature (second row) eigenmodes for a Reynolds number of 11,200. As we described in previous chapters, the turbulent transport of momentum is mainly influenced by large-scale structures which contain a large fraction of the kinetic energy. A qualitative comparison of dominant eigenfunctions of the momentum and scalar field reveals a characteristic distance between the centers of two neighboring high-temperature/low-temperature structures. The results show similar thermal and momentum structures and comparable spanwise scales in both fields. We further observe that high-temperature re-

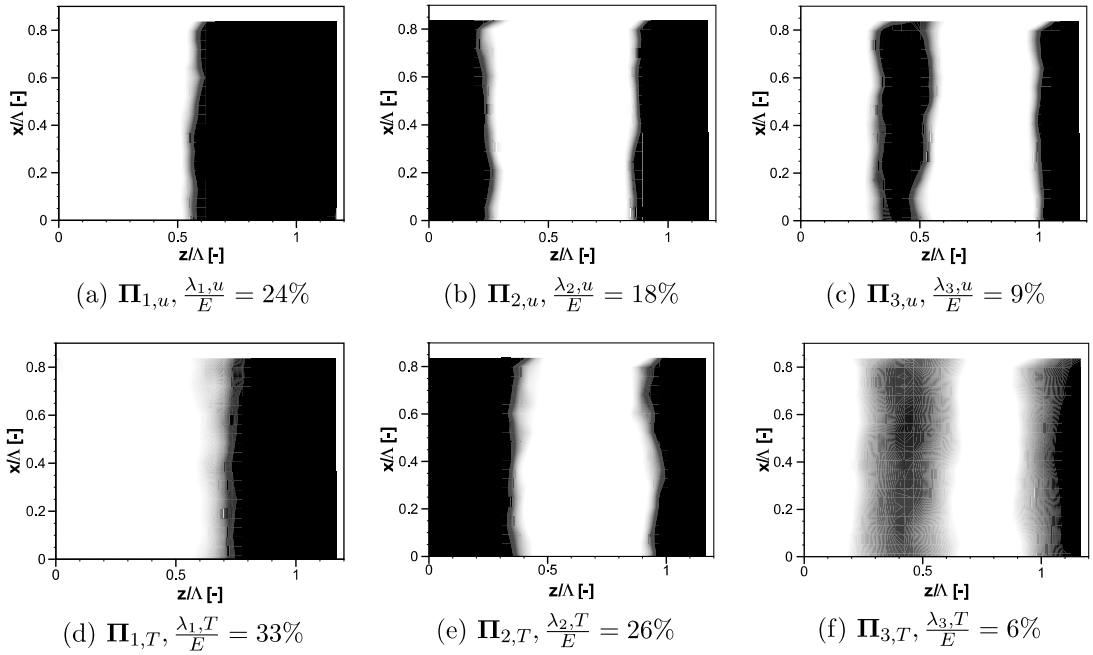

(a) $\mathbf{\Pi}_{1,u}$, $\frac{\lambda_{1,u}}{E} = 24\%$ (b) $\mathbf{\Pi}_{2,u}$, $\frac{\lambda_{2,u}}{E} = 18\%$ (c) $\mathbf{\Pi}_{3,u}$, $\frac{\lambda_{3,u}}{E} = 9\%$

(d) $\mathbf{\Pi}_{1,T}$, $\frac{\lambda_{1,T}}{E} = 33\%$ (e) $\mathbf{\Pi}_{2,T}$, $\frac{\lambda_{2,T}}{E} = 26\%$ (f) $\mathbf{\Pi}_{3,T}$, $\frac{\lambda_{3,T}}{E} = 6\%$

Fig. 7. Eigenfunctions of modes 1–3 from a decomposition of $u'/U_b(x,y/\Lambda = 0.26,z,t)$ and $T'/T_b(x,y/\Lambda = 0.26,z,t)$, FOV $= 0.83\Lambda \times 1.2\Lambda$, $Re_h = 11{,}200$, $Pr = 4.83$, $I = 220$ A.

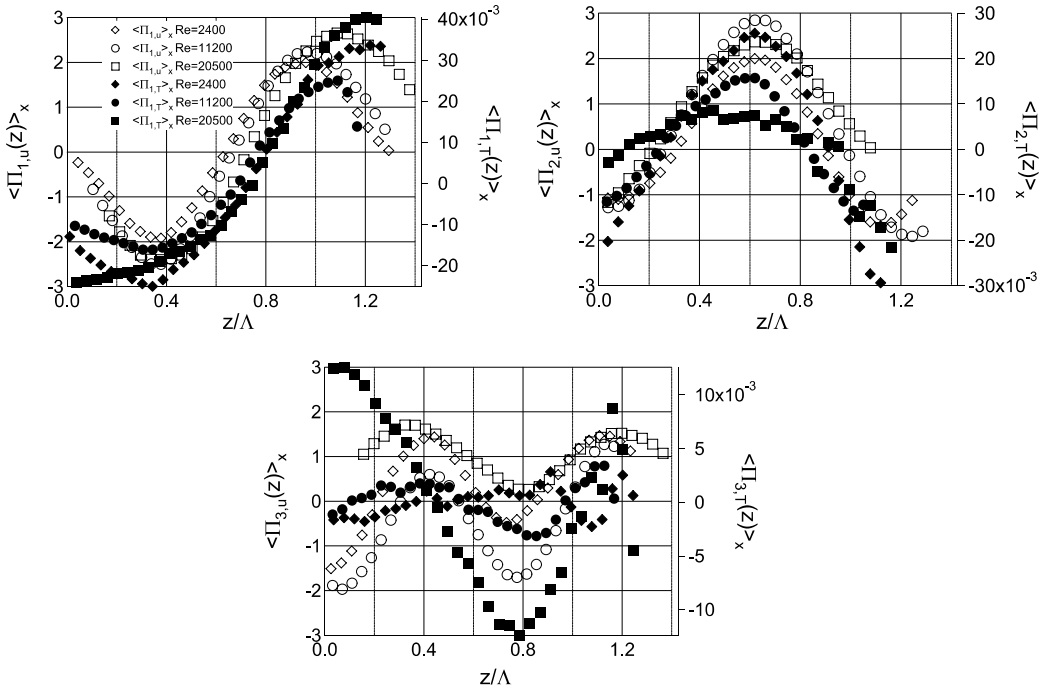

Fig. 8. Comparison of streamwise-averaged eigenfunctions $\mathbf{\Pi}_{1,T}$, $\mathbf{\Pi}_{2,T}$, $\mathbf{\Pi}_{3,T}$ and $\mathbf{\Pi}_{1,u}$, $\mathbf{\Pi}_{2,u}$, $\mathbf{\Pi}_{3,u}$ obtained for a decomposition of $u'/U_b(x, y/\Lambda = 0.26, z, t)$ and $T'/T_b(x, y/\Lambda = 0.26, z, t)$, $Pr = 4.83$, $I = 220$ A.

gions are mostly associated with low-momentum structures and low-temperature regions with high-momentum structures. The "energy" contained in the first dominant eigenmode of the temperature field ($\lambda_{1,T} = 0.33 \cdot E$) is significantly higher than that in the first velocity eigenmode ($\lambda_{1,u} = 0.24 \cdot E$).

Streamwise averaging of the calculated eigenmodes is used to detect the spanwise maximum and minimum location of each eigenfunction shown in Fig. 8. The characteristic spanwise scale Λ_z, and the location of maxima and minima, are identified and compared. The Reynolds numbers $Re_h = 2400$–$20{,}500$ provide a range of variation adequate to make a credible test of Reynolds number invariance.

In the considered Reynolds numbers range, the eigenfunctions $\mathbf{\Pi}_{u,1}$ and $\mathbf{\Pi}_{T,1}$, $\mathbf{\Pi}_{u,2}$ and $\mathbf{\Pi}_{T,2}$, $\mathbf{\Pi}_{u,3}$ and $\mathbf{\Pi}_{T,3}$ respectively, have similar characteristic scales, Λ_z, in the spanwise direction in the momentum and scalar field. The frequency and the location of the extrema of $\mathbf{\Pi}_{u,1}$ and $\mathbf{\Pi}_{T,1}$, $\mathbf{\Pi}_{u,2}$ and $\mathbf{\Pi}_{T,2}$ are similar. However, differences in the amplitudes of their oscillation exist. Further, no significant changes in the characteristic spanwise scale can be found in the first two streamwise-averaged velocity and temperature eigenmodes by altering Reynolds number. The results confirm a quantitative agreement of the frequency between thermal and momentum structures. The fourth and higher eigenfunctions do not have fixed spanwise coordinates and the deviation in the oscillation in momentum and scalar fields as well as Reynolds number effects are significant.

We calculate the eigenvalues $\lambda_{u,1}, \ldots, \lambda_{u,i}$ and $\lambda_{T,1}, \ldots, \lambda_{T,i}$ for the heated flow and compare them with the eigenvalues $\lambda_{u,1}, \ldots, \lambda_{u,i}$ for the unheated flow. Fig. 9 shows the fractional, cumulative energy to obtain a cumulative turbulent energy contribution of $0.85 \cdot E$ for $Re_h = 2400$ and $Re_h = 11{,}200$. The black circles denote the streamwise and spanwise velocity eigenvalues for the unheated flow. The blank circles are those for the heated flow. The number of velocity eigenmodes to obtain $0.85 \cdot E$ is smaller in the heated flow than the unheated one. The energy contained in the largest scales is significantly higher in the heated flow. The energy contained in the smaller scales is higher in the unheated flow. The eigenmodes of the streamwise velocity are the dominant contributors to the total kinetic energy. The dominance of the first most energetic eigenmodes increases with increasing Reynolds number by an order of magnitude. In the temperature field, the "energy" is contained in a small bandwidth of structures and more than half of it in the first two eigenmodes.

4. Results in the (x, y)-plane

4.1. Instantaneous velocity and temperature fields

We measure $M = 900$ realizations containing nine sequences of 100 simultaneous temperature and velocity fields in the (x, y)-plane. The normalized mean velocity and temperature profiles, $\bar{u}/U_B$, $\bar{v}/U_B$ and $\overline{T}/T_B$, are shown in Fig. 10 in wall-normal direction for $Re_h = 11{,}200$. We choose five characteristic streamwise positions; $x/\Lambda = 1.0$ and $x/\Lambda = 0$ (downstream) denote the wave crests, $x/\Lambda = 0.75$ and $x/\Lambda = 0.25$ (downstream) the reflections points, and $x/\Lambda = 0.5$ the wave trough. Due to the use of

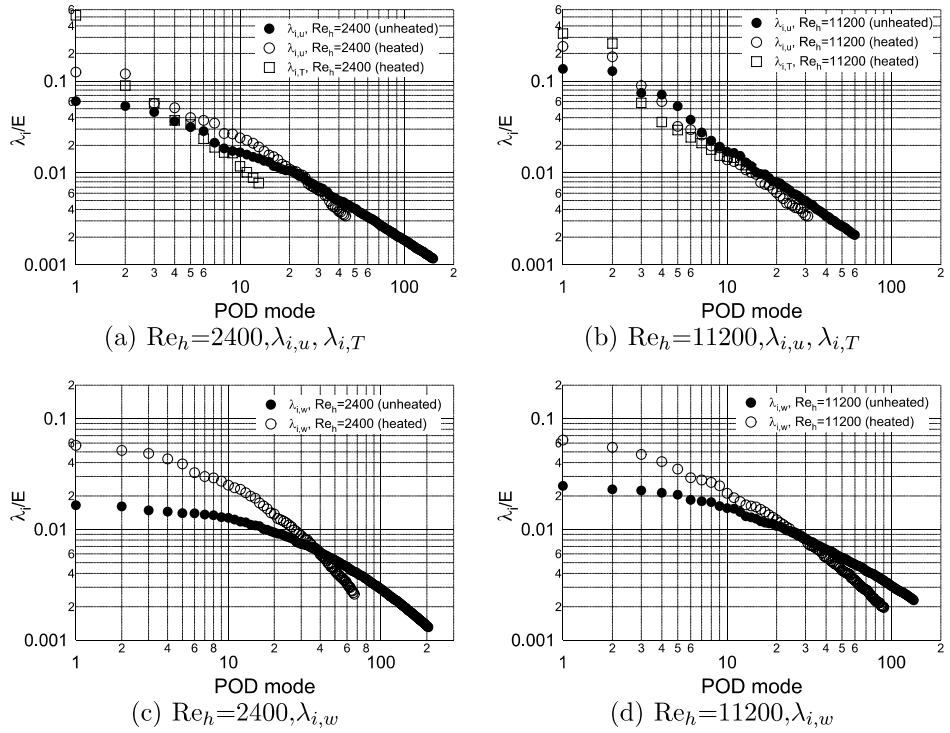

(a) Re_h=2400,$\lambda_{i,u}$, $\lambda_{i,T}$ (b) Re_h=11200,$\lambda_{i,u}$, $\lambda_{i,T}$

(c) Re_h=2400,$\lambda_{i,w}$ (d) Re_h=11200,$\lambda_{i,w}$

Fig. 9. Comparison of fractional energy contribution of velocity and temperature eigenmodes of non-heated and heated flow.

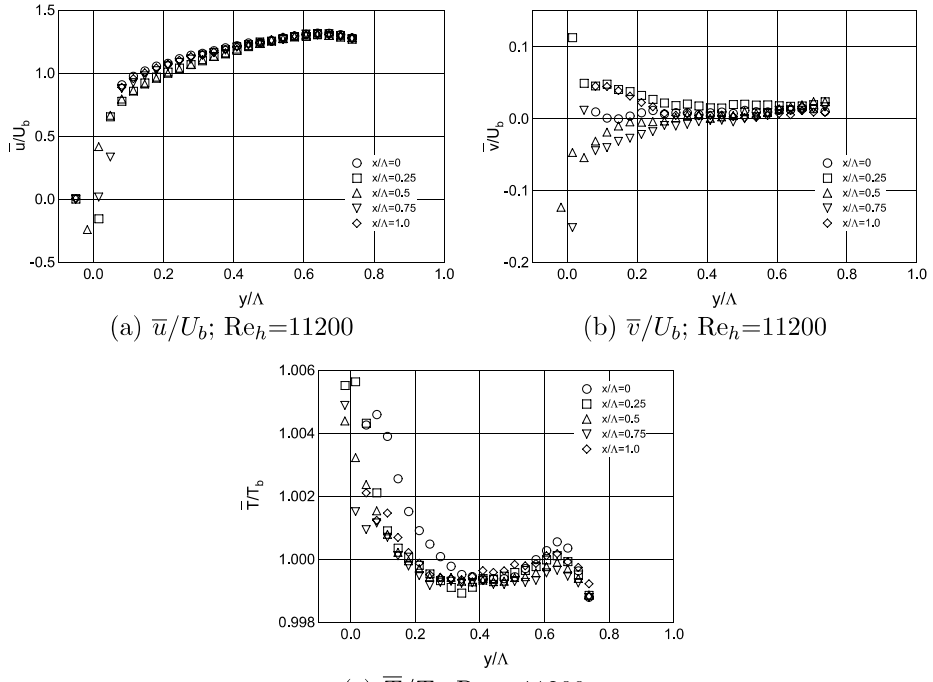

(a) $\overline{u}/U_b$; Re_h=11200 (b) $\overline{v}/U_b$; Re_h=11200

(c) $\overline{T}/T_b$; Re_h=11200

Fig. 10. Dimensionless mean velocity and temperature distributions in the wall-normal direction.

a telecentric lens on the 3-CCD color camera, the resolvable domain size is limited to FOV $= 0.83\Lambda \times 1.1\Lambda$.

Large distinct velocities are obtained close to the wall, values smaller than $U_\mathrm{b} = 0.71$ m/s for the streamwise velocity field and values larger than $T_\mathrm{b} = 29.46$ °C in the temperature field. At a wall-normal distance of $y/\Lambda = 0.6$, the temperature has a local maximum. The temperature increases as the flow convects downstream. The bulk temperature is obtained at a wall-normal location, that is slightly below the location of the bulk velocity. The

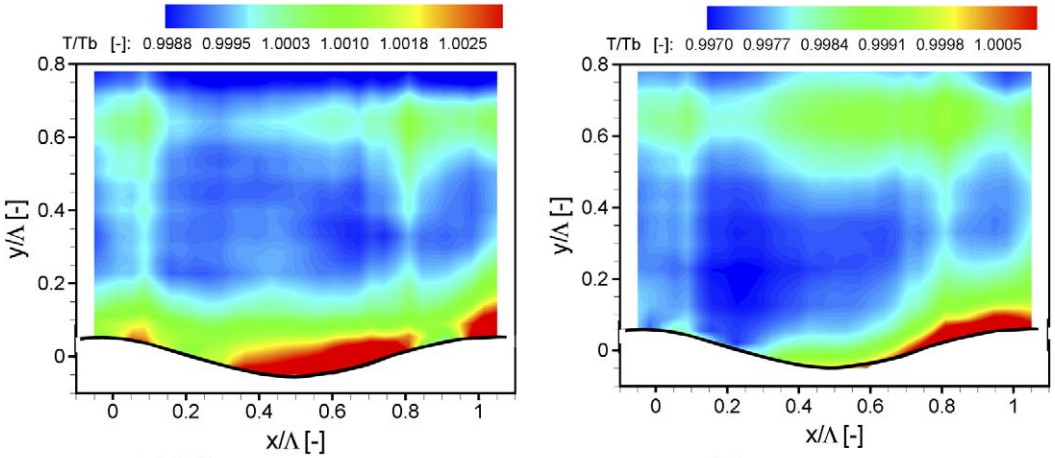

(a) $\overline{T}/T_b$; Re_h=11200 (b) $\overline{T}/T_b$; Re_h=20500

Fig. 11. Contour plots of the dimensionless temperature $\overline{T}/T_\mathrm{b}$.

wall-normal velocity has large negative values in the separation region and large positive values in the upslope region close to the wall. The normal velocity and temperature profiles highly depend on the streamwise location for $y/H < 0.4$, the streamwise velocity for $y/H < 0.1$.

To discuss transport phenomena in heated flow over waves, we consider spatial information of two-dimensional contour plots of the dimensionless mean temperature at Reynolds numbers of 11,200 and 20,500 shown in Fig. 11(a) and (b). For $Re_\mathrm{h} = 11{,}200$, high temperature values are found close to the wall. The temperature decreases rapidly from the wall in the normal direction between $0.2 < y/H < 0.5$. We observe large temperature values in the separation region at $Re_\mathrm{h} = 20{,}500$. Further, large temperature gradients are seen in the region of negative shear stress. Surprisingly, we observe a region between $0.5 < y/H < 0.7$, where the temperature increases again and achieves a local maximum. The region of large temperature values close to the wall is connected directly to those regions of increased temperature fluid in the outer region. The elongated region in the outer flow becomes larger with increasing Reynolds number.

Instabilities in the flow enhance the heat transfer through macroscopic bulk fluid mixing which reduces temperature gradients. These instabilities are neither simple spanwise vortices nor near-vertical vortex pairs, but are complex, three-dimensional elongated rotating high-temperature low-momentum structures established above the train of sinusoidal waves. The large-scale counter-rotating vortices appear to be identical with those that were found in the (y_β, z)-plane under isothermal conditions [20] that can be related to a Craik–Leibovich type 2 (CL2) instability [21]. Those angular momentum structures transport warm fluid away from the wall and interrupt efficiently the boundary layer. The structures replace it with fluid from the core, thereby creating a fresh boundary layer that has increased near-wall temperature gradients. The areas of higher temperature values close to the wall and in the outer region encloses streamwise oriented motion of low-temperature high-momentum fluid. Both "mechanisms" are self-sustaining.

We calculate second-order turbulence quantities to provide quantitative information on the structure of the instantaneous velocity and temperature field. Fig. 12 shows the longitudinal and wall-normal velocity and temperature fluctuation intensities, $\sqrt{\overline{u'^2}}/U_\mathrm{b}$, $\sqrt{\overline{v'^2}}/U_\mathrm{b}$, and $\sqrt{\overline{T'^2}}/T_\mathrm{b}$, at five different characteristic streamwise locations. Under the

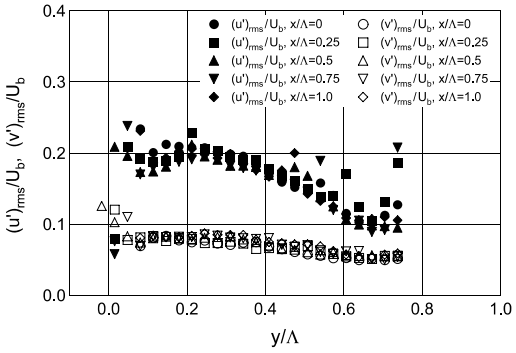

(a) $\sqrt{\overline{u'^2}}/U_b$, $\sqrt{\overline{v'^2}}/U_B$

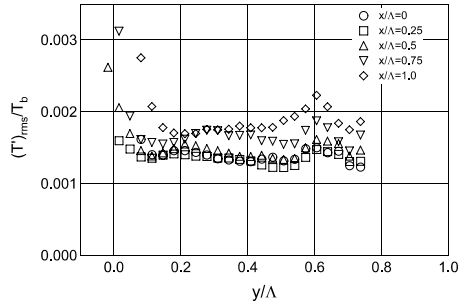

(b) $\sqrt{\overline{T'^2}}/T_b$

Fig. 12. Dimensionless mean velocity and temperature distributions $\sqrt{\overline{u'^2}}/U_\mathrm{b}$, $\sqrt{\overline{v'^2}}/U_\mathrm{b}$, and $\sqrt{\overline{T'^2}}/T_\mathrm{b}$, $Re_\mathrm{h} = 11{,}200$.

present experimental conditions of constant wall heat flux, the wall temperature fluctuation can be recognized as the fluctuation of the local heat transfer coefficient. The wall-normal velocity fluctuation is of prime interest close to the wall, since it is the flow component which is expected to contribute largely to the convection of heat and momentum from one stratum of fluid to another. Streamwise and wall-normal velocity fluctuations are almost independent of the streamwise position, and therefore of the wall roughness, in the outer region for $y/\Lambda > 0.2$. The streamwise fluctuations are large in the outer region between $0 < y/\Lambda > 0.4$ and decrease close to the wall. The profiles show a local maximum at $y/\Lambda = 0.2$. In contrast, the wall-normal fluctuation intensities are small in the outer region and increase close to the wall. The temperature profiles depend on the streamwise location. We obtain large intensities close to the wall and confirm the previous found local maxima at $y/H = 0.6$. The temperature fluctuation intensities at $y/H = 0.6$ decrease as the flow convects downstream. The temperature fluctuations correlate with the wall-normal velocity fluctuations close to the wall.

We calculate the cross-correlation coefficients R_{uv}, R_{uT}, and R_{vT} for $Re_h = 11{,}200$ and $Re_h = 20{,}500$, that define the degree of similarity between those quantities (Fig. 13). For smooth pipe flow turbulence, Bremhorst and Bullock [22] obtained a close agreement between R_{vT} and R_{uv}. Subramanian and Antonia [23] confirmed the results for boundary layer flows and Iritani [24] for flows between smooth walls and proposed that the wall-normal turbulent heat flux and the Reynolds shear stress are generated by similar turbulence mechanisms. The mechanisms of generating turbulence found for smooth walls or pipes are expected to be different to the processes for flow over heated wavy walls. However, the correlation coefficient R_{vT} agrees roughly with $-R_{uT}$ and R_{uv} for $y/\Lambda < 0.5$, shown in Fig. 13. Hence, the correlation indicates a degree of similarity between momentum and heat transport mechanisms.

A good correlation between u' and T' is obtained at a wall-normal location of $y/\Lambda = 0.1$. This is in accord with the observed association of low- and high-velocity structures with high- and low-temperature regions, respectively. In comparison to literature data over smooth walls, where the coefficient $-R_{uT}$ was found to be approximately 1 close to the wall, the coefficient only reaches a maximum value of 0.9 over the rough wall. This might be due to the breakdown of the structures by the roughness and the absence of wall streaks.

The heat flux can be defined as the energy in transit owing to a temperature difference per unit cross-sectional area normal to the direction of the flux. We consider the turbulent streamwise and wall-normal heat flux in Fig. 14. The heat flux components are shown in wall-normal direction at a Reynolds number of 11,200. The black circles present the streamwise heat flux with its axis on the left side, the blank circles illustrate the wall-normal heat flux with its axis on the right side.

The similarities in the co-spectra of v' and T', u' and T', can also be found in the turbulent heat flux. Close to the wall the fluxes increase significantly, obtain a maximum at $y/\Lambda = 0.1$ and decrease to a value of zero at the wall. The region cannot be fully resolved due to the size of the interrogation area. Further, the fluxes obtain a local maxima at $y/\Lambda = 0.6$. The absolute values of the streamwise and wall-normal heat flux highly correlate for $y/\Lambda > 0.2$. When the streamwise heat flux decreases, the normal heat flux increases and vice versa. The ratio of normal to streamwise heat flux is $\mathcal{O}\{-0.06\}$. The streamwise flux dominates the transport of heat in the bulk flow. Close to the wall, the contribution of the wall-normal flux to the total flux increases significantly to a ratio of $\mathcal{O}\{0.13\}$. In the outer region, the vertical flux of heat is inhibited by the reduction of $\overline{v'^2}$.

The spatial evolution of the heat flux components is shown in Fig. 15. Large values for the streamwise and normal heat flux are obtained in the region of flow separation and reattachment for $x/\Lambda = 0.25$ and $x/\Lambda = 0.75$. We observe positive values of the normal heat flux in the separated region and negative values at $x/\Lambda = 0.25$. The relative contribution of the normal heat flux to the total heat flux is large for $y/\Lambda < 0.2$.

Fig. 16 investigates how the magnitude of the turbulent heat flux depends on the Reynolds number. The streamwise heat flux in Fig. 16(a) shows Reynolds number dependency in the outer region for $y/\Lambda > 0.5$. The largest values are obtained at $Re_h = 15{,}500$ and $Re_h = 5600$ at $y/\Lambda = 0.1$,

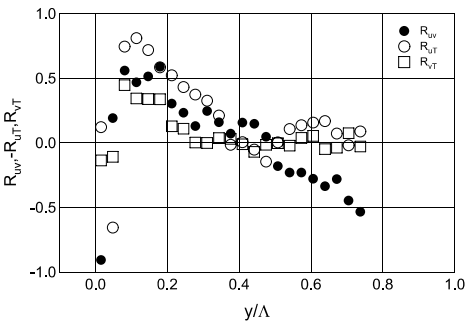

Fig. 13. Turbulent momentum and heat transfer cross-correlation coefficients, $x/\Lambda = 0.75$, $Re_h = 11{,}200$.

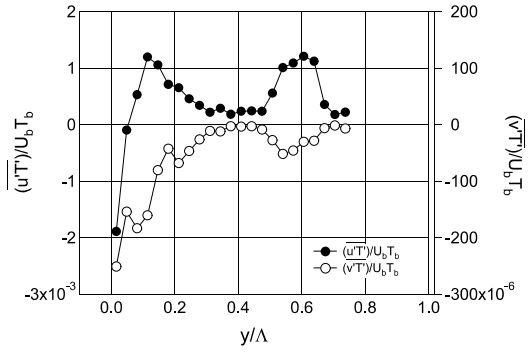

Fig. 14. Turbulent heat fluxes, $\overline{u'T'}$ and $\overline{v'T'}$, in the (x,y)-plane, $x/\Lambda = 0.25$, $Re_h = 11{,}200$, $Pr = 4.83$, $I = 220$ A.

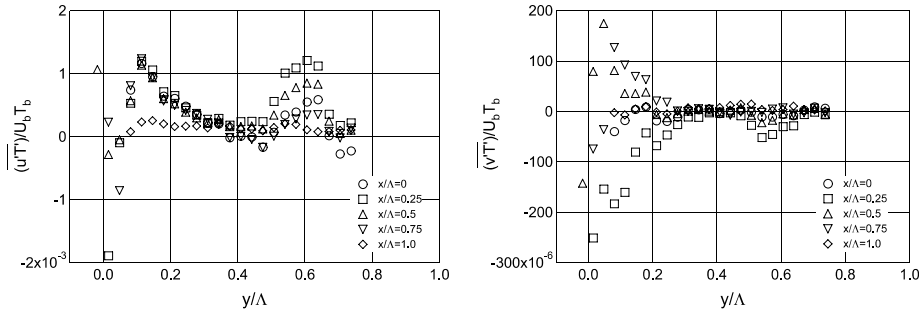

(a) $\overline{u'T'}/(U_bT_b)$ (b) $\overline{v'T'}/(U_bT_b)$

Fig. 15. Spatial evolution of streamwise and normal heat flux, $Re_h = 11{,}200$.

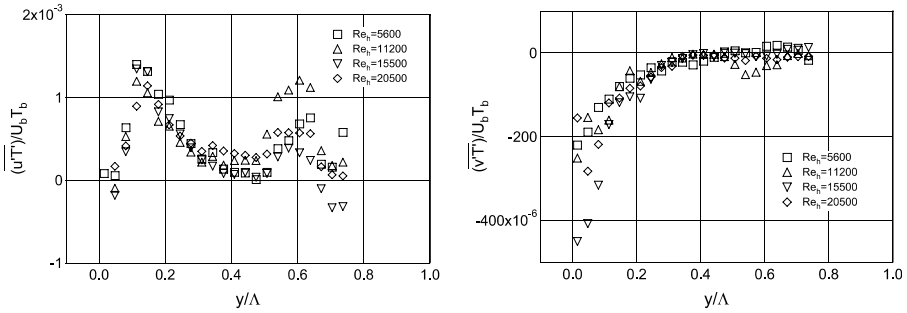

(a) $\overline{v'T'}/U_bT_b$ (b) $\overline{u'T'}/U_bT_b$

Fig. 16. Reynolds number dependency of the streamwise and normal heat flux at $x/\Lambda = 0.25$.

and at $Re_h = 11{,}200$ in the outer region at $y/\Lambda = 0.6$. The normal heat-flux is almost independent of the Reynolds number for $0.2 < y/\Lambda < 0.45$. We observe the largest total heat flux at $Re_h = 11{,}200$ at the wall-normal location $y/\Lambda = 0.55$. In agreement with the findings in the streamwise direction, the largest flux at $y/\Lambda = 0.05$ is found at $Re_h = 15{,}500$. We suggest that neither the transport of the wall-normal scalar flux, nor the streamwise flux can be significantly enhanced by increasing Reynolds number, if the forced flow is turbulent. The transfer of heat has an optimum at a specific Reynolds number (approximately at $Re_h \approx 11{,}200$) in the turbulent regime, and is not further enhanced.

4.2. Structural information from POD analysis

We use the method of snapshots and perform a proper orthogonal decomposition (POD) on the streamwise velocity and temperature fields in the (x, y)-plane. The results are compared for different Reynolds numbers at a fixed streamwise location ($x/\Lambda = 0.5$) in wall-normal direction. The comparison is shown for the first three eigenmodes in Fig. 17. The first eigenmodes, $\mathbf{\Pi}_{1,u}$ and $\mathbf{\Pi}_{1,T}$, are highly correlated for the momentum and scalar field and different Reynolds numbers. At higher eigenmodes the correlation reduces rapidly. The dominant process is the transport of low-momentum high-temperature fluid from the heated wall to the bulk. This, in turn, replaces high-momentum cold fluid which, if it convects towards the wall, will result in the reverse process. If the two processes occur at almost the same time, a good correlation between heat and momentum is obtained. For smaller structures identified by higher order eigenmodes the process is considerably less organized so that high momentum fluid is not always cold fluid and vice versa. Thus, it results in a considerably lower correlation between longitudinal velocity and temperature fluctuations.

We calculate velocity and temperature eigenvalues for the heated flow and compare those with the velocity eigenvalues for the unheated flow. The fractional, cumulative energy to obtain 85% of the total turbulent energy E is shown in Fig. 18 for $Re_h = 2400$ and $Re_h = 11{,}200$. The first dominant streamwise velocity eigenmodes in Fig. 18(a) and (b) contain more energy in the heated flow than in the unheated flow case, and the number of eigenmodes (to obtain $0.85 \cdot E$) is smaller. The dominance of the first eigenmodes increases with increasing Reynolds number. The spectrum of the normal velocity fluctuations for the unheated and heated flow cases in Fig. 18(c) and (d) shows a shift of energy in the heated flow situation to higher eigenmodes. The bulk of the energy of the normal velocity fluctuation is concentrated in lower order eigenmodes in comparison to the distribution of the temperature fluctuations. Hence, the spectra of temperature fluctuations are quite different from those of the normal velocity fluctuations but similar to the spectra of the longitudinal velocity

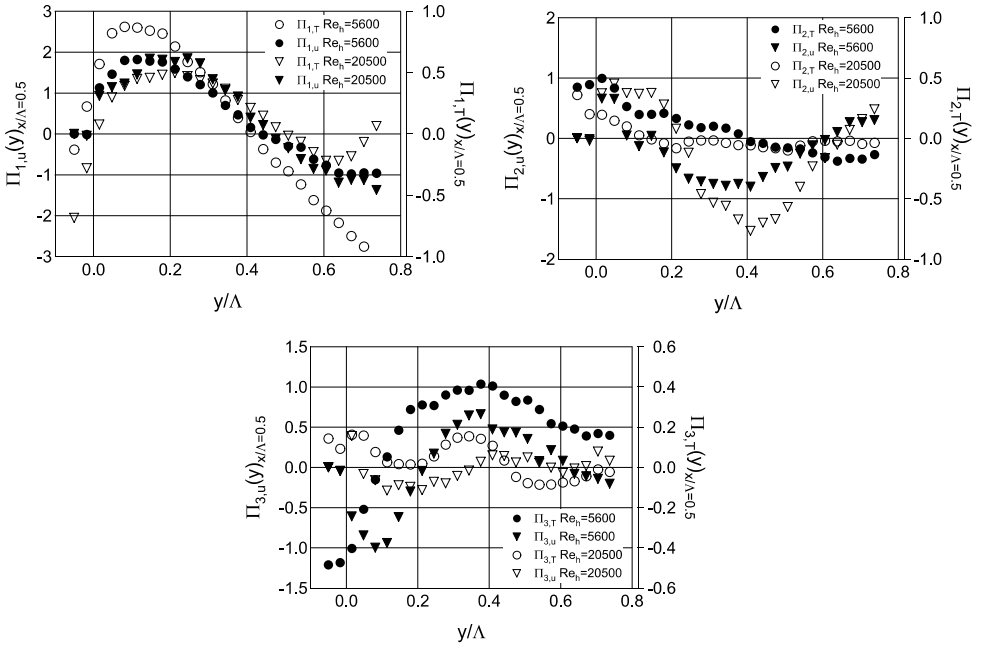

Fig. 17. Comparison of eigenfunctions $\mathbf{\Pi}_{1,T}$, $\mathbf{\Pi}_{2,T}$, $\mathbf{\Pi}_{3,T}$ and $\mathbf{\Pi}_{1,u}$, $\mathbf{\Pi}_{2,u}$, $\mathbf{\Pi}_{3,u}$ obtained for a decomposition of $u'/U_b(x/\Lambda = 0.5, y, z, t)$ and $T'/T_b(x/\Lambda = 0.5, y, z, t)$, $Pr = 4.83$, $I = 220$ A.

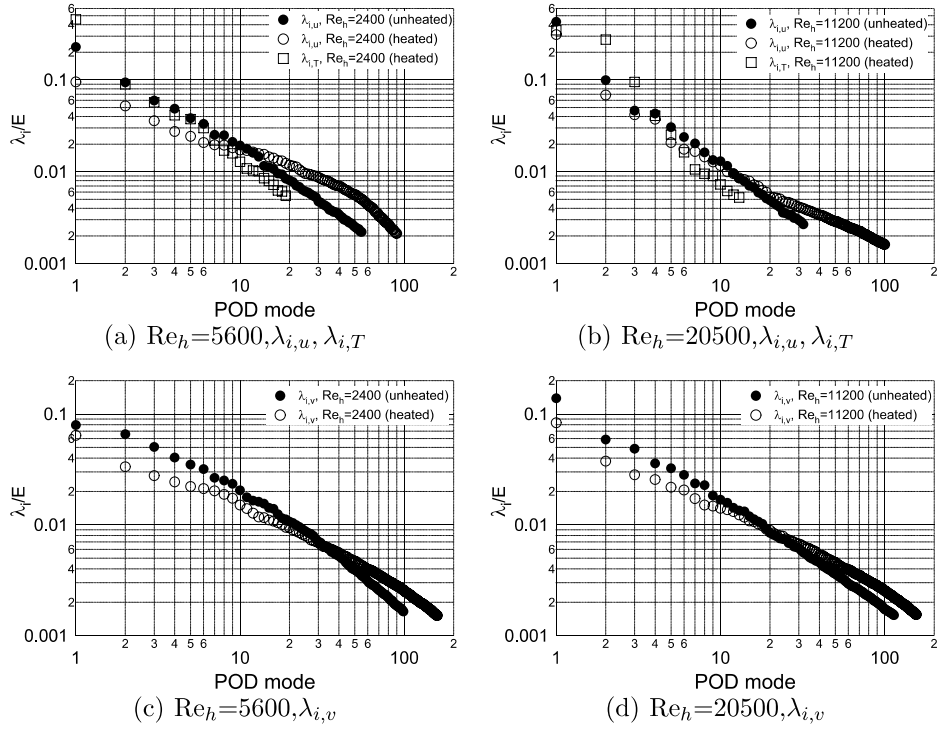

Fig. 18. Comparison of fractional energy contribution of velocity and temperature eigenmodes of non-heated and heated flow.

fluctuations (for lower order eigenmodes) as would be expected from the analogy between heat and momentum transfer. It is further emphasized by the spectral correlation coefficients.

Power spectra for u'/U_b and v'/U_b suggest, that smaller scale motion is the main contributor to $\sqrt{\overline{v'^2}}$. The contributions to $\overline{v'T'}$ and $\overline{u'v'}$ are about four times the contributions to $\sqrt{\overline{v'^2}}$.

Fig. 19 displays the energy distribution of different scales for $\overline{u'T'}$ and $\overline{v'T'}$. Large-scale structures contribute significantly to $\overline{u'T'}$, smaller scales of motion are more important contributors to $\overline{v'T'}$.

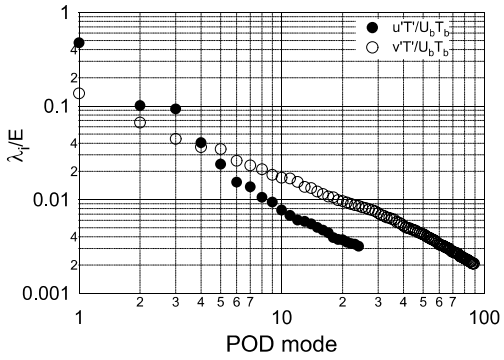

Fig. 19. Comparison of energy spectra for wall-normal and streamwise heat flux.

5. Concluding remarks

We demonstrated the applicability of a combined particle image velocimetry and liquid crystal thermometry technique to access the turbulent heat flux, $\overline{u_i'T'}$, in a flow over heated waves.

From measurements in the (x,z)-plane, we observed that large-scale longitudinal structures carry the bulk of the kinetic energy in the momentum and scalar fields. In the (x,y)-plane, we found a process of low-momentum high-temperature fluid coming from the heated wall replacing high-momentum lower-temperature fluid, which convects towards the wall. If this mechanism occurs at almost the same time, a perfect correlation between heat and momentum is obtained. For smaller structures identified by higher order eigenmodes, the process is less organized so that high momentum fluid is not always cold fluid and vice versa. This causes a considerably lower correlation between longitudinal velocity and temperature fluctuation. The mechanism of transferring near-wall high-temperature fluid to the outer region is found to be three-dimensional. The heat transfer enhancement close to the wall is a result of complex interactions between the core fluid and the boundary-layer fluid through shear-layer destabilization and self-sustaining oscillations.

A proper orthogonal decomposition of velocity and temperature fields reveals quantitative agreement between large-scale thermal and momentum structures, whereas at higher eigenmodes the correlation reduces rapidly. We confirm a characteristic spanwise scale, Λ_z, in both fields. Significant Reynolds number effects are seen in the high frequency eigenvalues, and therefore in the amplitude of the oscillation of smaller scale structures. The total energy associated with those eddies is small and has a negligible effect on the total energy of the turbulence. The observation is important, since it documents the same mechanism on transport of heat and momentum at different Reynolds numbers through largest structures.

The distribution of budget terms of the streamwise and wall-normal heat fluxes, $\overline{u'T'}$ and $\overline{v'T'}$, are similar to those for the two Reynolds stress components, $\overline{u'u'}$ and $\overline{u'v'}$. Over the channel cross-section, the wall-normal heat flux is by an order of magnitude smaller than the streamwise heat flux. Co-spectra of v' and T', u' and T' indicate that larger scale structures make a significant contribution to $\overline{u'T'}$ and smaller scales of motion are more important contributors to $\overline{v'T'}$.

Acknowledgements

We gratefully acknowledge financial support from the Swiss National Science Foundation (SNF).

References

[1] B.E. Launder, On the computation of complex heat transfer in complex turbulent flows, Int. J. Heat Transfer 110 (1988) 1112–1128.
[2] M. Matsumura, R.A. Antonia, Momentum and heat transport in the turbulent intermediate wake of a circular-cylinder, J. Fluid Mech. 259 (1993) 651–668.
[3] D. Dabiri, M. Gharib, Digital particle image thermometry: the method and implementation, Exp. Fluids 11 (1991) 77–86.
[4] A. Günther, Large-scale structures in Rayleigh–Bénard convection and flow over waves, Ph.D. thesis, ETH Zurich, Switzerland, 2001.
[5] A. Günther, Ph. Rudolf von Rohr, Structure of the temperature field for flow over heated waves, Exp. Fluids 33 (2002) 920–930.
[6] N. Kruse, Isothermal and non-isothermal flow over solid waves: transport and structure, Ph.D. thesis, ETH Zurich, Switzerland, 2005.
[7] R.J. Adrian, Particle-imaging techniques for experimental fluid mechanics, Ann. Rev. Fluid Mech. 23 (1991) 261–304.
[8] J. Westerweel, Fundamentals of digital particle image velocimetry, Meas. Sci. Technol. 8 (1995) 1379–1392.
[9] M. Raffel, C. Willert, J. Kompenhans, Particle image velocimetry. A practical guide, Springer, 1998.
[10] H.G. Park, D. Dabiri, M. Gharib, Digital particle image velocimetry/thermometry and application to the wake of a heated cylinder, Exp. Fluids 30 (2001) 327–338.
[11] A. Günther, Ph. Rudolf von Rohr, Large scale structures in a developed flow over a wavy wall, J. Fluid Mech. 478 (2003) 257–285.
[12] A. Günther, Ph. Rudolf von Rohr, Influence of the optical configuration on temperature measurements using fluid-dispersed TLCs, Exp. Fluids 32 (2002) 533–541.
[13] S. Funatani, N. Fujisawa, T. Takano, T. Matsuura, Simultaneous measurement of temperature and velocity by liquid crystal visualization combined with scanning light sheet technique, J. Visualization Soc. Jpn. 19 (Suppl. 1) (1999) 259–262.
[14] D.J. Farina, J.M. Hacker, R.J. Moffat, J.K. Eaton, Illuminant invariant calibration of thermochromic liquid crystals, Exp. Thermal Fluid Sci. 9 (1994) 1–12.
[15] R.J. Moffat, Describing the uncertainties in experimental results, Exp. Thermal Fluid Sci. 1 (1988) 3–317.
[16] J.L. Lumley, Similarity and turbulent energy spectrum, Phys. Fluids 10 (4) (1967) 855.
[17] Z.-C. Liu, R.J. Adrian, T.J. Hanratty, Large-scale modes of turbulent channel flow: transport and structure, J. Fluid Mech. 448 (2001) 53–80.
[18] G. Berkooz, P. Holmes, J.L. Lumley, The proper orthogonal decomposition in the analysis of turbulent flows, Ann. Rev. Fluid Mech. 25 (1993) 539–575.
[19] L. Sirovich, Turbulence and the dynamics of coherent structures. Pt I. Coherent structures, Quart. Appl. Math. XLV (1987) 561–571.
[20] N. Kruse, A. Günther, Ph. Rudolf von Rohr, Dynamics of large-scale structures in a turbulent flow over waves, J. Fluid Mech. 485 (2003) 87–96.

[21] R.W.C. Phillips, Z. Wu, On the instability of wave-catalysed longitudinal vortices in strong shear, J. Fluid Mech. 272 (1994) 235–254.
[22] K. Bremhorst, K.J. Bullock, Spectral measurements of turbulent heat and momentum transfer in fully developed pipe flow, Int. J. Heat Mass Transfer 16 (1973) 2141–2154.
[23] C.S. Subramanian, R.A. Antonia, Effect of Reynolds number ion slightly heated turbulent boundary layer, Int. J. Heat Mass Transfer 24 (1981) 1833–1846.
[24] Z. Iritani, Heat flux in turbulent flow between smooth walls, Int. J. Heat Fluid Flow 13 (1992) 340–346.